J Eng Math (2011) 71:205–222
DOI 10.1007/s10665-010-9442-4

Meshless study of dynamic failure in shells

J. Liu

Received: 16 January 2010 / Accepted: 22 November 2010 / Published online: 22 December 2010

Abstract The dynamic fracture of a thin-walled structure that is mainly due to impact and explosive loading is studied. Use is made of a meshless SPH shell formulation based on Mindlin–Reissner's theory. The formulation is an extension of the continuum-corrected and stabilized SPH method allowing a thin structure to be modelled using only one particle characterizing the mean position of the shell surface. Fracture is based on an effective criterion similar to that of the visibility method. Four numerical examples are studied among which tearing of pre-notched plates, fracture due to impact loading and dynamic fracture of cylindrical shells.

Keywords Dynamic fracture · Explosion · Impact · Shell · Smoothed Particle Hydrodynamics (SPH)

1 Introduction

Modeling of cracks [1] in thin structures poses particular challenges for numerical methods, particularly in extreme events such as structures undergoing blast and detonation loading [2]. Meshless methods are good candidates to predict complex phenomena involving large deformations and fracture. The authors believe that, due to the absence of a mesh, meshless methods have advantages over finite-element methods since they do not rely on a background mesh making them attractive for analyzing problems involving large deformations including complex failure patterns and fragmentation [3,4]. Connectivities between neighboring nodes are easily and efficiently broken.

The origins of meshless methods were laid in the seventies [5] and these methods have grown in popularity since, especially in the nineties. One of the earliest and most efficient meshless methods is the Smoothed Particle Hydrodynamics (SPH) method [6]. Since SPH is based on the strong formulation of the problem, it has two major disadvantages, namely numerical instabilities and insufficient polynomial order of completeness. While the first drawback is attributed to the collocation procedure, the second drawback is SPH-specific. Classical SPH formulations cannot represent even a constant function properly and results deteriorate when unstructured meshes are used. Therefore, corrected SPH methods have been developed that address this inconsistency [7–10]. Most of these referenced contributions improved the consistency of the SPH method up to first-order. In other words, corrected SPH versions are capable of reproducing linear fields at least for a gradient correctly. Numerical instabilities were extensively studied, e.g. by [11–18], and there exist different techniques to get rid of them. Two very popular

J. Liu (✉)
Department of Mechanical Engineering, Beijing University of Technology, Beijing, People's Republic of China
e-mail: sajaliu@hotmail.com

techniques are stabilized conforming nodal integration and adding stress points to the collocation points where the linear momentum equation is enforced. Different implementations exist for the latter method.

Classical SPH is a continuum-based method. However, in the case of thin structures, three-dimensional continuum formulations are inefficient. Some meshless formulations for thin structures exist [19–24] but they are all based on weak formulations and computationally more expensive than SPH.

In this paper, we study detonation-driven fracture of thin pipes with a SPH shell method. Therefore, we adopt a normalized and stabilized continuum formulation [13] (see also [25]) in the context of the Mindlin–Reissner shell theory [26]. We present an effective fracture model similar to the visibility method [27]. The most pertinent features of our method are its robustness, simplicity and computational efficiency.

The main contribution is the development and the implementation of a new and simple fracture method into an SPH shell formulation. To the best of our knowledge, this is the first time that such a fracture-based shell formulation has been applied to the failure of thin shells due to blast loading.

2 SPH method

An approximation of a function $\mathbf{u}$ at the position $\mathbf{X}_I$ in the SPH formulation is given by

$$\mathbf{u}(\mathbf{x}_I) = \mathbf{u}_I = \sum_{J=1}^{M} N_{IJ}\mathbf{u}_J, \tag{1}$$

where $\mathbf{u}(\mathbf{X}_I) = \mathbf{u}_I$ is the node of interest, $\mathbf{u}_J$ are neighboring nodal parameters, M is the number of neighboring particles and $N(\mathbf{X}_I - \mathbf{X}_J) = N_{IJ}$ are SPH shape functions; see Fig. 1; capital indices refer to node numbers and for the sake of conciseness we introduce the following abbreviations for a quantity f: $f(\mathbf{X}_I) = f_I$, $f(\mathbf{X}_I - \mathbf{X}_J) = f_{IJ}$. In the classical SPH theory, the shape functions N_{IJ} are calculated as the product of the particle volume V_J associated with particle J and the weighting function $W(r_{IJ}, h)$ that depends on the distance $r_{IJ} = \mathbf{X}_I - \mathbf{X}_J$ between particles I and J:

$$N_{IJ} = V_J \; W(r_{IJ}, h_{IJ}). \tag{2}$$

The parameters $h_{IJ} = h_I - h_J$, h_I and h_J determine the size of the domain of influence of particles I and J, respectively (Fig. 1); h_{IJ} is called the dilation parameter. Generally, compactly supported kernel functions are used in order to optimize efficiency. The volume V_J at particle J, needed in Eq. 2, can be obtained from Voronoi techniques as illustrated in Fig. 2 for the special case of a structured equispaced particle arrangement. Details on the construction of Voronoi cells can be found in the literature on meshfree methods [17,28].

Our weighting function is the commonly used cubic B-spline:

$$W(r_{IJ}, h) = W(s) = \begin{cases} 1 - 6s^2 + 8s^3 - 3s^4 & s \le 1 \\ 0 & s > 1 \end{cases}, \quad s = \frac{\mathbf{X}_I - \mathbf{X}_J}{2h} \tag{3}$$

that has circular support size; $\mathbf{X}_I$ and $\mathbf{X}_J$ denote the material coordinates of particle I and J. The description of the weighting function in material coordinates is essential for the stability of a particle method [17]. Gradients of functions in SPH formulation are approximated by

$$\nabla\mathbf{u}_I = \sum_{J=1}^{M} \nabla N_{IJ} \otimes \mathbf{u}_J, \tag{4}$$

where M denotes the number of neighboring particles with $N_{IJ} \neq 0$ and ∇N_{IJ} are the derivatives of the shape functions. Since SPH does not even fulfill zero-order completeness [29–31], a so-called symmetrization is performed by adding the term $-\nabla N_{IJ} \otimes \mathbf{u}_I$ to Eq. 4 yielding

$$\nabla\mathbf{u}_I = \sum_{J=1}^{M} \nabla N_{IJ} \otimes (\mathbf{u}_J - \mathbf{u}_I); \tag{5}$$

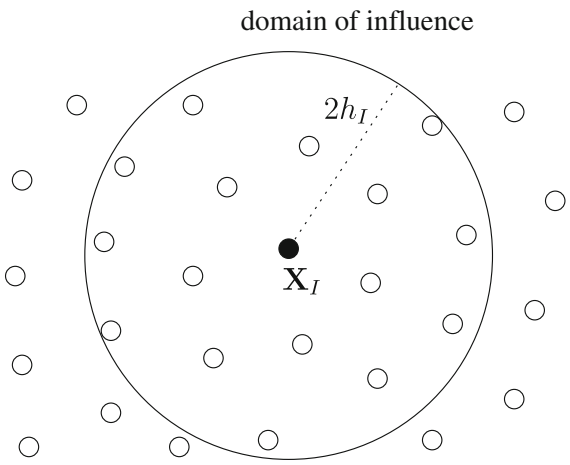

Fig. 1 Domain of influence of particle *I*

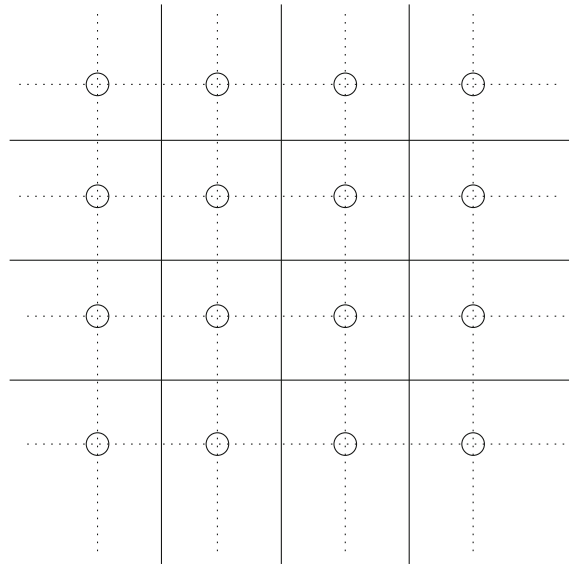

Fig. 2 Voronoi diagram for a structured equispaced particle arrangement

this obviously ensures that SPH fulfills zero-order completeness for the derivatives. First-order completeness is not achieved in classical SPH. This means that the gradient of a constant field cannot be enforced at the boundaries of the volume and that linear strain fields cannot be reproduced exactly. The corrected SPH formulation we adopted is based on re-normalization of derivatives of the shape functions [13] and modifies Eq. 5 with a correction matrix **B**:

$$\nabla \mathbf{u}_I = \sum_{J=1}^{M} \nabla N_{IJ} \otimes (\mathbf{u}_J - \mathbf{u}_I) \cdot \mathbf{B}, \tag{6}$$

$$\mathbf{B} = \mathbf{H}^{-1}, \tag{7}$$

$$\mathbf{H} = \sum_{J=1}^{M} (\mathbf{X}_J - \mathbf{X}_I) \otimes \nabla N_{IJ}, \tag{8}$$

which is constructed so that (6) fulfills first-order completeness. Defining

$$\nabla \hat{N}_{IJ} = \nabla N_{IJ} \cdot \mathbf{B}, \tag{9}$$

we can rewrite (6) as follows:

$$\nabla \mathbf{u}_I = \sum_{J=1}^{M} \nabla \hat{N}_{IJ} \otimes (\mathbf{u}_J - \mathbf{u}_I)\,. \tag{10}$$

The conservation of linear momentum in the absence of body forces is given by

$$\varrho \ddot{\mathbf{u}} = \nabla \cdot \mathbf{P}, \tag{11}$$

where ϱ denotes the density in the current configuration, **P** is the stress tensor, **u** the displacement vector and superimposed dots denote material time derivatives. The corrected formulation is given by

$$\varrho \ddot{\mathbf{u}}_I = \sum_{J=1}^{M} (\mathbf{P}_J - \mathbf{P}_I) \cdot \nabla \hat{N}_{IJ}. \tag{12}$$

Since the early studies of [5,6,10,32,33], it is well known that numerical instabilities occur in collocation-based meshfree methods as shown e.g. by [17,28]. This instability is comparable to the numerical instability due

Fig. 3 SPH shell particle

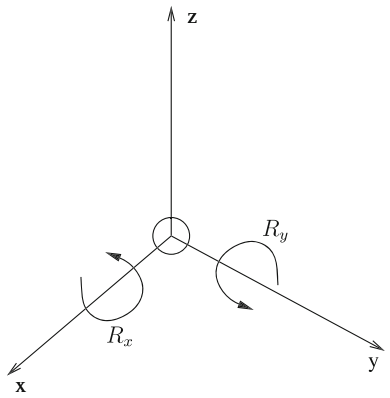

to under-integration in the weak formulation [28]. Adding additional points, so-called stress points eliminate this instability. As the name may suggest, only stresses are computed at the stress points. Kinematic quantities such as the displacement field or the velocity field are interpolated. We adopt the stress-point technique described in [13] and add stress points in order to avoid numerical instabilities. Stress points are moved by simple approximation with the meshfree shape functions. The linear momentum equation is then enforced at the stress points rather than the particles:

$$\varrho \ddot{\mathbf{u}}_I = \sum_{K=1}^{N_S} (\mathbf{P}_K - \mathbf{P}_I) \cdot \nabla \hat{N}_{IK}. \tag{13}$$

In Eq. 13, N_S denotes the set of all stress points.

3 SPH shell formulation

We now present the SPH Mindlin–Reissner shell formulation. Therefore, only particles on the mean surface are discretized. The particles have two rotational (no drilling rotation) and three translational degrees of freedom; see Fig. 3. Each point on the mean plane is assigned a thickness. The position vector in the initial configuration $\mathbf{X}$ of any point M located at a distance ξ from the mean plane can be expressed as

$$\mathbf{X} = \mathbf{X}_M + \xi \mathbf{n}_0 \tag{14}$$

with $\xi \in [-0.5t, 0.5t]$, t being the thickness of the shell; $\mathbf{n}_0$ is the initial normal vector that represents the orientation of the material with respect to the mean plane and $\mathbf{X}_M$ are points on the mean surface. Similarly, we obtain the displacement vector as follows,

$$\mathbf{u} = \mathbf{u}_M + \xi\,(\mathbf{n} - \mathbf{n}_0), \tag{15}$$

with $\mathbf{n}_0$ being the pseudo-normal vector in the initial configuration. The technique for updating $\mathbf{n}$ will be described later.

Firstly, we define the local coordinate system associated with the shell in the initial configuration that will be subsequently denoted by L_0. The initial local coordinates $\mathbf{x}_{L_0}$ of each point are defined from the general initial coordinates $\mathbf{x}_0$ through a rotation matrix,

$$\mathbf{x}_0 = \mathbf{G}_0^{-1} \cdot \mathbf{x}_{L_0}, \tag{16}$$

where the rotation matrix is obtained via the matrix multiplication $\mathbf{G} = \mathbf{R}_x\,\mathbf{R}_y\,\mathbf{R}_z$ with

$$\mathbf{R}_x = \begin{bmatrix} 1 & 0 & 0 \\ 0 & \cos\alpha & \sin\alpha \\ 0 & -\sin\alpha & \cos\alpha \end{bmatrix} \quad \mathbf{R}_y = \begin{bmatrix} \cos\beta & 0 & \sin\beta \\ 0 & 1 & 1 \\ -\sin\beta & 0 & \cos\beta \end{bmatrix} \quad \mathbf{R}_z = \begin{bmatrix} \cos\gamma & -\sin\gamma & 0 \\ -\sin\gamma & \cos\gamma & 0 \\ 0 & 0 & 1 \end{bmatrix}. \tag{17}$$

With these definitions, the displacement vector in (15) can be rewritten as

$$\mathbf{u}(x_{L_0}, y_{L_0}) = \mathbf{u}_M(x_{L_0}, y_{L_0}) + z_{L_0}\left(\mathbf{n}(x_{L_0}, y_{L_0}) - \mathbf{n}_0(x_{L_0}, y_{L_0})\right). \tag{18}$$

In L_0 , one calculates the total Lagrangian NSPH shape functions N_{L_0} leading to the expression of the gradient of a field in the global coordinate system L_G:

$$\nabla u = \mathbf{G}_0 \cdot \nabla_{L_0} u, \tag{19}$$

$$(\nabla u)_j = \mathbf{G}_{0ji} \cdot (\nabla_{L0} u)_i = G_{0ji} \cdot \sum_{k=1}^{N} (N_{,xiL0})_k \cdot u_k = \sum_{k=1}^{N} (N'_{,x0})_k \cdot u_k \tag{20}$$

with

$$(N'_{,x0})_k = G_{0ji} \cdot (N_{,xi_{L0}})_k. \tag{21}$$

Now, one can define the gradient matrix $\mathbf{F}$ for any point in the shell including for a point on the mean plane ($z_{L_0} = \xi = 0$):

$$\mathbf{F} = \mathbf{G}_0 \cdot \mathbf{F}_3 \tag{22}$$

with

$$\mathbf{F}_3 = \begin{bmatrix} x_{,x_{L_0}} & x_{,y_{L_0}} & n_x \\ y_{,x_{L_0}} & y_{,y_{L_0}} & n_y \\ z_{,x_{L_0}} & z_{,y_{L_0}} & n_z \end{bmatrix}. \tag{23}$$

We now express the Cauchy strain tensor for small strains:

$$E_{ij} = 0.5\left(u_{i,j} + u_{j,i}\right) = E_{Mij} + E_{Bij}(\xi) \tag{24}$$

with

$$E_{Mij} = 0.5\left(u_{Mi,j} + u_{Mj,i}\right) \tag{25}$$

and

$$E_{Bij}(\xi) = \frac{\xi}{2}\left(\Delta n_{i,j} + \Delta n_{j,i}\right) \tag{26}$$

with $\Delta\mathbf{n} = \mathbf{n} - \mathbf{n}_0$. As indicated by the above equations, $\mathbf{E}$ is divided into a part $\mathbf{E}_M$ which is constant throughout the thickness, associated with membrane and transverse shear effects, and a part $\mathbf{E}_B(\xi)$ which is linear throughout the thickness, associated with bending effects. For geometrical nonlinear applications (especially for large rotations), the usual nonlinear membrane strains are added to the linear membrane ones. The nonlinear bending and shear strains are neglected. Then, strains must be written in the local coordinate system of the current position of the mean plane of the plate, denoted by L_C , in order to calculate the stresses in agreement with the plane-stress assumption. In order to define this coordinate system, one determines two vectors $\mathbf{n}'_2$ and $\mathbf{n}_2$ of the mean plane. The normal $\mathbf{n}_3$ to the plane is obtained by the vector cross-product of $\mathbf{n}'_2$ and $\mathbf{n}_2$

$$\mathbf{n}'_2 = \frac{\partial \mathbf{X}(x_L, y_L)}{\partial x_L}, \tag{27}$$

$$\mathbf{n}_2 = \frac{\partial \mathbf{X}(x_L, y_L)}{\partial y_L}, \tag{28}$$

$$\mathbf{n}_3 = \mathbf{n}'_2 \times \mathbf{n}_2. \tag{29}$$

The basis is completed with a third vector:

$$\mathbf{n}_1 = \mathbf{n}_3 \times \mathbf{n}_2. \tag{30}$$

Using these three basis vectors, a rotation matrix $\mathbf{G}_L$ is defined that connects the current local system L_C to the global system L_G. One should note that in the case of an updated Lagrangian formulation in which the reference

configuration is regularly updated, the equality $\mathbf{G}_0 = \mathbf{G}_L$ holds. The expression of the local membrane shear strains ϵ_{L_M} and bending strains ϵ_{L_B} are as follows:

$$\epsilon_{L_M} = \mathbf{G}_L \cdot \mathbf{F}^{-t} \cdot \mathbf{E}_M \cdot \mathbf{F}^{-1} \cdot \mathbf{G}_L^T, \tag{31}$$

$$\epsilon_{L_B} = \mathbf{G}_L \cdot \mathbf{F}^{-t} \cdot \mathbf{E}_B \cdot \mathbf{F}^{-1} \cdot \mathbf{G}_L^T, \tag{32}$$

where $\mathbf{F}$ is the deformation gradient which can be rewritten, still in the L_C coordinate system, in the form of generalized strain vectors ϵ_g and ϵ_s defined by:

$$\epsilon_g = \begin{pmatrix} \epsilon_{L_{m_{xx}}} \\ \epsilon_{L_{m_{yy}}} \\ \epsilon_{L_{m_{xy}}} \\ \epsilon_{L_{f_{xx}}} \\ \epsilon_{L_{f_{yy}}} \\ \epsilon_{L_{f_{xy}}} \end{pmatrix}, \quad \epsilon_s = \begin{pmatrix} \epsilon_{L_{s_{xz}}} \\ \epsilon_{L_{s_{yz}}} \\ 0 \end{pmatrix}. \tag{33}$$

The generalized stress vectors σ_g and σ_s are obtained accordingly. The membrane and shear-stress resultants N_{ij} and S_i, along with the bending moments m_{ij}, are obtained by integration through the thickness which leads to the following relationship between the stress resultant and the generalized stress vector:

$$\begin{aligned} N_{ij} &= t\sigma_{L_{m_{ij}}}, \quad i, j = x, y, \\ S_i &= t\sigma_{L_{s_{iz}}}, \quad i, j = x, y, \\ m_{ij} &= \frac{t^3}{12}\sigma_{L_{b_{ij}}}, \quad i, j = x, y. \end{aligned} \tag{34}$$

With Hooke's law for plane-stress conditions, we can express the nominal stress tensor $\mathbf{P}$ by

$$\mathbf{P} = \mathbf{G}_L^T \cdot \mathbf{S} \cdot \mathbf{G}_L \cdot \mathbf{F}^T = \mathbf{s} \cdot \mathbf{F}^T \tag{35}$$

with

$$\mathbf{S} = \begin{bmatrix} N_{xx} & N_{xy} & T_x \\ N_{xy} & N_{yy} & T_y \\ T_x & T_y & 0 \end{bmatrix}. \tag{36}$$

Similar to the 3D case, the membrane and transverse-shear equilibrium equation are as follows:

$$\mathbf{P}^T \cdot \nabla = \varrho \ddot{\mathbf{u}}, \tag{37}$$

where superimposed dots denote material time derivatives. Next, the angular accelerations $\ddot{\theta}_{x_L}$ and $\ddot{\theta}_{y_L}$ are calculated using the two moment equilibrium equations defined in the local coordinate system by

$$\mathcal{I} \cdot \ddot{\theta}_{x_L} = m_{yy,y} + m_{xy,x} + t \cdot \sigma_{yz}, \qquad \mathcal{I} \cdot \ddot{\theta}_{y_L} = m_{xx,x} + m_{xy,y} - t \cdot \sigma_{xz} \tag{38}$$

or in matrix form

$$\mathcal{I} \cdot \ddot{\theta}_L = \mathbf{L}\,\mathrm{div}\,(\mathbf{m}) + \mathbf{T}_L = \mathbf{L} \cdot \mathbf{m}^T \cdot \nabla_L + \mathbf{T}_L, \tag{39}$$

with t being the shell's thickness and the rotation moment of inertia $\mathcal{I}$ and

$$\mathbf{L} = \begin{bmatrix} 0 & 1 & 0 \\ 1 & 0 & 0 \\ 0 & 0 & 0 \end{bmatrix}, \quad \mathbf{T}_L = \begin{bmatrix} t \cdot \sigma_{yz} \\ -t \cdot \sigma_{xz} \\ 0 \end{bmatrix}, \quad \mathbf{m} = \begin{bmatrix} m_{xx} & m_{xy} & 0 \\ m_{xy} & m_{yy} & 0 \\ 0 & 0 & 0 \end{bmatrix}. \tag{40}$$

Equation 39 can be also obtained in the L_G coordinate system by

$$\mathcal{I}_0 \cdot \ddot{\theta} = \mathbf{M}^T \cdot \nabla_0 + \mathbf{T}_0, \tag{41}$$

with $\mathcal{I}_0 = \mathcal{I}$ and

$$\mathbf{M} = J \cdot \mathbf{F}^{-1} \cdot \mathbf{G}_L^T \cdot \mathbf{m} \cdot \mathbf{L}^T \cdot \mathbf{G}_L, \quad \mathbf{T}_0 = J \cdot \mathbf{G}_L \cdot \mathbf{T}_L. \tag{42}$$

Thus, $\mathbf{M}$ is the equivalent for the bending stresses of the nominal stress tensor $\mathbf{P}$ for the stresses that are constant throughout the thickness. Hence, we finally obtain:

$$\mathcal{I}_0 \cdot \ddot{\theta} = \sum_{J=1}^{N} (\mathbf{M}_J - \mathbf{M}_I) \nabla N_{0IJ} + \mathbf{T}_0, \quad \varrho \cdot \ddot{\mathbf{u}} = (\mathbf{P}_J - \mathbf{P}_I) \nabla N_{0IJ}. \tag{43}$$

The vector of angular accelerations $\ddot{\theta}$ thus obtained is used to update $\mathbf{n}$. Now we consider the rotation of $\mathbf{n}$ with respect to its initial position $\mathbf{n}_0$. Therefore, a different rotation matrix (compared to $\mathbf{G}_L$) is needed that is denoted here by $\mathbf{G}_n^t$. Its increment $\Delta\mathbf{G}_n$ expresses the rotation of $\mathbf{n}$ during a time step. Using θ, one determines the incremental rotation vector $\Delta\theta$ that defines the rotation of $\mathbf{n}$ during a time step, owing to time integration. The corresponding rotation matrix $\Delta\mathbf{G}_n$ is then calculated using the Rodrigues formula:

$$\mathbf{G}_n^{t+\Delta t} = \Delta\mathbf{G}_n \cdot \mathbf{G}_n^t, \qquad \mathbf{n}^{t+\Delta t} = \mathbf{G}_n^{t+\Delta t} \cdot \mathbf{n}_0. \tag{44}$$

4 Artificial viscosity

For problems involving shock waves, additional numerical problems occur. Shock waves result in discontinuities in the velocity field at the shock front as well as discontinuities in the pressure (and energy) field. Although it is theoretically possible to capture the shock waves, we decided to use an artificial viscosity that smears the shock front over a very small region. The artificial viscosity also eliminates oscillations at the shock front and was extensively studied in the context of the SPH method [6,7,10,13,32,34]. Meanwhile, several different artificial viscosities are used in SPH methods. We adopt the artificial viscosity proposed by [35] defined by

$$P_{vIJ} = \varrho_{IJ}^2 \left(-\alpha\, d\, c\, \mu_{IJ} + \beta\, d^2\, \mu_{IJ}^2\right), \tag{45}$$

where the parameters α and β are set equal to 0.1 and 1.1, respectively; c is the speed of sound and

$$\mu_{IJ} = \frac{(\mathbf{v}_I - \mathbf{v}_J) \cdot \mathbf{r}_{IJ}}{r^2 + \epsilon}, \quad \mathbf{r}_{IJ} = \frac{\mathbf{X}_I - \mathbf{X}_J}{|\mathbf{X}_I - \mathbf{X}_J|}, \tag{46}$$

where r is the distance between particles I and J and the parameter ϵ is set to 0.1 times the square of the dilation parameter h in order to avoid singularities; $\mathbf{v}_I$ and $\mathbf{v}_J$ denote the velocity vector of the particles I and J, respectively. The force on the particle I due to the viscous pressure is then computed by

$$\mathbf{f}_v = \frac{m_i}{\varrho_i} \cdot \nabla P_v = h \cdot S_i \cdot \mathbf{F}^{-1} \nabla P_v = h \cdot s_i \cdot \mathbf{F}^{-1} \sum_{j=1}^{N} P_{vij} \nabla N_{ij}. \tag{47}$$

More details on the derivation of the viscosity are given in the above-mentioned SPH literature.

Within the shell-formulation framework, the effect of this viscosity concerns the membrane alone and it does not involve the out-of-plane component of the velocities. This type of damping constitutes the right choice for fluids because one should not create artificial shear stresses that could perturb the flow. In the case of shells, this type of viscosity cannot control instability modes involving the normal velocities with respect to the tangent plane. Therefore, Monaghan's viscosity was expanded to generate viscous shear stresses as well. In the simple 2D case of a beam, this viscous stress is

$$\tau = \eta \frac{\partial(\mathbf{v} \cdot \mathbf{n}_3)}{\partial x} \tag{48}$$

with $\eta = \gamma \varrho h\, c$, where γ is a calibration parameter set to 0.2. The simplified expression of this transverse shear stress is

$$\tau_{ij} = \eta \frac{\left(\mathbf{v_i} - \mathbf{v}_j\right) \cdot \mathbf{n}_3)}{x_i - x_j}. \tag{49}$$

In the case of a 3D plate, τ_{ij} becomes a tensor τ_{ij} involving only transverse shear stresses. Thus, it can be expressed in the local coordinate system by

$$\tau_{ij} = \eta \frac{\left(\mathbf{v_i} - \mathbf{v}_j\right) \cdot \mathbf{n}_3)}{x_i - x_j} \begin{bmatrix} 0 & 0 & 1 \\ 0 & 0 & 0 \\ 1 & 0 & 0 \end{bmatrix}. \tag{50}$$

The viscous force can be expressed by

$$\mathbf{f}_{sij} = h \cdot S_i \cdot \mathbf{F}^{-1} \cdot \tau_{gij} \cdot \nabla N_{ij}, \tag{51}$$

where τ_{gij} corresponds to the viscous stress tensor expressed in the global coordinate system. It can be shown that for the total viscous force $\mathbf{f}_{tv} = \mathbf{f}_v + \mathbf{f}_s$, $\mathbf{f}_{vij} \neq \mathbf{f}_{vji}$ and hence we use a symmetrization:

$$\hat{\mathbf{f}}_{vij} = 0.5 \left(\mathbf{f}_{vij} + \mathbf{f}_{vji}\right). \tag{52}$$

5 Constitutive model and fracture criterion

In this manuscript, we use a standard elasto–plastic constitutive model as explained in detail in many references [36,37], [38, Sect. 5], [39,40]. The main assumption here is that the entire section becomes plastic at once; this assumption is true when the shell is subject to membrane loads alone.

We now propose an effective fracture model that is similar to the visibility method [29,41–45]. Since only one particle is used over the thickness, fracture occurs over the entire thickness. The Rankine criterion is used to detect the onset of fracture [46–52] although more-complex criteria, such as loss of stability, might be studied in the future [53,54]. We do not use cohesive-zone models after a discrete crack is introduced which will be a subject for future study as well. Subsequently, we propose an effective implementation of discrete cracks in the context of meshfree methods.

The discontinuous displacement field is achieved by excluding particles on the opposite side of the crack surface as in the visibility method; see Fig. 4. Therefore the crack is considered to be opaque and the SPH approximation becomes:

$$u^h(\mathbf{X}) = \sum_{W^+} N_I(\mathbf{X}) \mathbf{u}_I, \tag{53}$$

where W^+ is the set of particles on the same side of the crack. As noted in (53), we choose the initial configuration that facilitates the re-approximation that can be difficult when quantities are considered in the deformed configuration. The major difficulty with problems involving moving cracks is due to re-approximation and the re-configuration of the material. The visibility method [44] is one of the most widely used methods to model and represent cracks in meshless methods among others [55,56]. However, the visibility method has certain drawbacks. First of all, the visibility method introduces undesired discontinuities [57,58] that fortunately do not affect the convergence of the method [29]. Secondly, while the implementation of the visibility method in two dimensions is straightforward, it can become cumbersome in three dimensions. To conclude, the major source of these drawbacks is related to the search algorithm and the re-approximation. Therefore, we propose a simpler method that is very similar to the visibility method since it considers the crack as opaque as well.

Since we assume only through-the-thickness cracks, we take advantage of the 2D implementation. For cylindrical shells we will be concerned with later, we use the visibility method in the parent domain. Moreover, we use a simple node-splitting algorithm to represent the crack surface. Therefore, the two-dimensional crack surface is represented by pairs of piece-wise straight lines as shown in Fig. 5. The nodes on the crack surface are marked as square black boxes, except at the crack tip, whereas the other nodes are represented as hollow circles. In previous meshless approaches, when a crack grows, the crack surface is reconstructed by adding new nodes. Here, we propose to attach the crack tip to an existing material/interpolation node which simplifies the implementation tremendously. A similar approach was proposed by Rabczuk and Belytschko [46] with the cracking-particle method. However, in

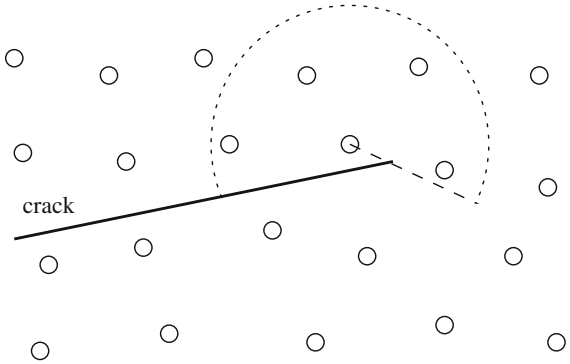

Fig. 4 Modification of domain of influence in order to model a discontinuous displacement field

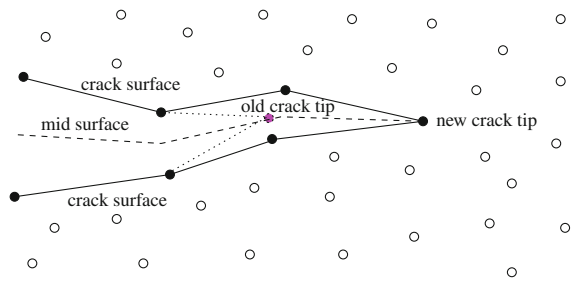

Fig. 5 Numerical scheme to model crack growth

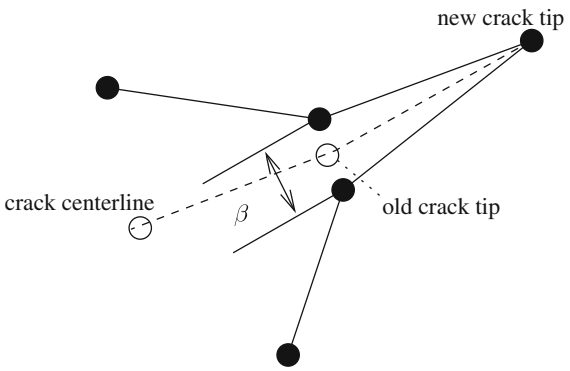

Fig. 6 Crack splitting scheme

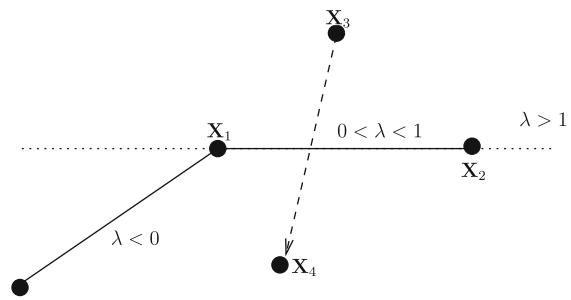

Fig. 7 Effective implementation of the visibility criterion

contrast to Rabczuk and Belytschko [46], we preserve the continuity of the crack surface. As shown in Fig. 5, the crack tip only moves from one particle to another.

Subsequently, we describe the splitting scheme in more detail. We first have to distinguish between crack nucleation and crack propagation. A crack propagates from an existing crack tip, when the cracking criterion is fulfilled at a certain distance from that crack tip. We opt to check this criterion within a radius r around the crack tip. For crack nucleation, we control the crack length that is coupled to the underlying discretization.

For crack propagation that is the usual case for the applications discussed in this manuscript; we also control the crack length and the orientation of the crack is determined by the Rankine criterion although more-complex criteria than stated above can be used. Once a new crack tip is obtained, we split the old crack tip into two points that have the same values of the field variables at that particular time. The kinematic quantities such as the displacement field of the added node are then given by

$$\mathbf{u}_{\text{new1}} = \mathbf{u}_{\text{old}} + \beta, \qquad \mathbf{u}_{\text{new2}} = \mathbf{u}_{\text{old}} - \beta \tag{54}$$

with $\beta \ll \mathbf{u}_{\text{old}}$. The value β serves only the purpose of making a physical distinction between the two new nodes once they are separated; see also Fig. 6.

As stated above, the discontinuous displacement field is achieved through exclusion of nodes located on the opposite side of the crack surface and therefore the crack is considered to be opaque as shown in Fig. 7. Here, we propose an effective implementation of this check (whether or not a node is located on the same side of the crack) with respect to a given straight crack segment. Therefore we check whether or not the straight crack segment, shown as dashed line in Fig. 7, intercepts different particles in the vicinity of the crack.

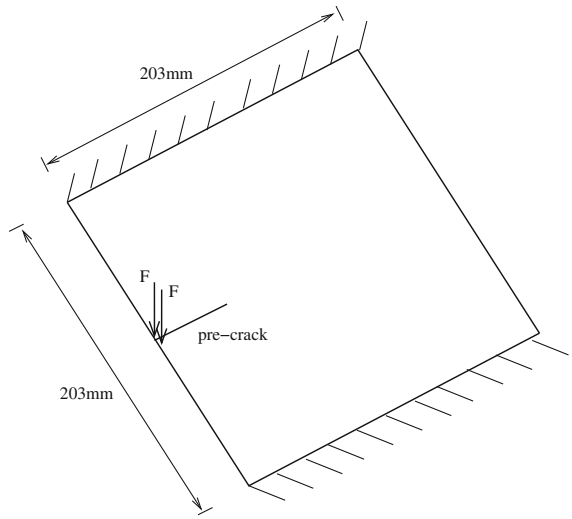

Fig. 8 Tearing of a pre-cracked plate

Since the crack propagation is incremental, one only needs to check and modify a limited number of nodes in the current crack-tip area, which is defined as the union of two circles centered at the current crack tip and at the next crack tip. To modify the meshless connectivity map, this check needs to be performed only inside the union of two circles, $\mathcal{R} = \mathcal{R}_1 \bigcup \mathcal{R}_2$.

Let us consider Fig. 7 and let us assume that we want to modify the connectivity relation between particle $\mathbf{X}_3 \in \mathcal{R}$ and the rest of the particles inside $\mathcal{R}$. Let an arbitrary point inside $\mathcal{R}$ be $\mathbf{X}_4$ and the new and old crack tip be $\mathbf{X}_1$ and $\mathbf{X}_2$, respectively. The equations of the straight line that connects the points $\mathbf{X}_3$ and $\mathbf{X}_4$ are given by:

$$\mathbf{X} = \mathbf{X}_3 + \lambda_1 \ (\mathbf{X}_4 - \mathbf{X}_3) \tag{55}$$

and the equations of the straight line that connects the points $\mathbf{X}_1$ and $\mathbf{X}_2$ are given by:

$$\mathbf{X} = \mathbf{X}_1 + \lambda_2 \ (\mathbf{X}_2 - \mathbf{X}_1) \tag{56}$$

with the two unknown parameters λ_1 and λ_2 used to identify whether or not the two lines have intersections. The above equations can be solved with respect to the unknown parameters. When $0 < \lambda_1 < 1$ and $0 < \lambda_2 < 1$, then the two lines have intersections. When the two lines (from $\mathbf{X}_1$ to $\mathbf{X}_2$ and from $\mathbf{X}_3$ to $\mathbf{X}_4$) are parallel, then the determinant of the 2×2 matrix from the above system of equations is zero. If the above condition is met, then one should disconnect the connection between these two points and the node is no longer in the set of nodes W^+, Eq. 53.

6 Numerical results

6.1 Tearing of pre-cracked plate

Tearing of plates was experimentally studied by [59]. The experiment consists of pre-crack elastic plates with different pre-crack lengths, Fig. 8. The test involves large displacements and rotations. The thickness of the plate is 0.8 mm. The material parameters are Young's modulus $E = 210$ GPa, Poisson's ratio $\nu = 0.3$ and yield strength is 306 MPa.

We show results for two pre-crack lengths: 30 and 60 mm. Different meshes were studied, starting from 10,000 nodes up to almost 100,000 nodes. The force–displacement curves for the pre-cracked plates with 60 mm pre-crack and different particle arrangements are shown in Fig. 9b. The displacement is measured at the location where the

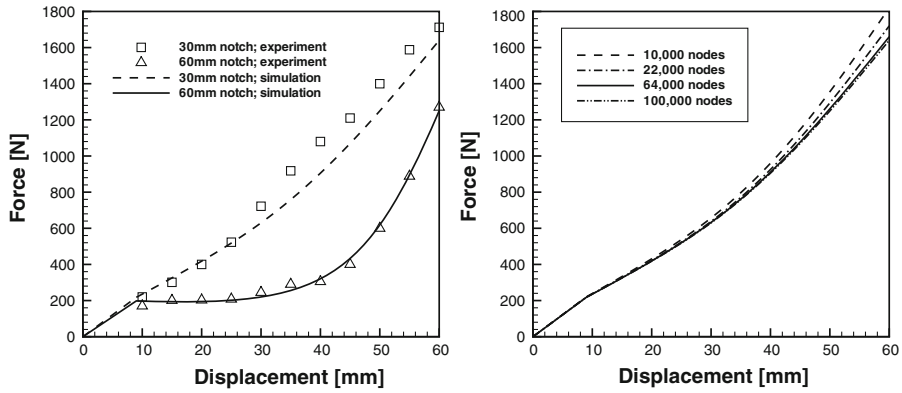

(a) Experiment vs. simulation **(b)** Mesh-refinement

Fig. 9 Tearing of pre-cracked plates; **a** Results of the 30 and 60 mm pre-notched crack and mesh-refinement study

load is applied. When more than 64,000 nodes are used, the results become independent of the discretization. In the context of the FEM, this is usually referred to as mesh-independence. Figure 9a compares the experimental result with the numerical simulation for the finest discretization. The agreement is excellent.

6.2 Impact problem

This problem shows the power of our method when applied to more-complex situations. We study the impact of a spherical projectile onto a 20 mm thick square plate. The velocity of the impactor is 400 m/s and the material parameters are taken from the previous section.

Different discretizations were studied, starting from 10,000 nodes up to almost 100,000 nodes. The displaced plate after 200 μs is shown in Fig. 10. We see that the results do not depend on the number of nodes. The diameter of the crater is almost the same for 10,000 nodes and 100,000 nodes. Also four petals are observed in both discretizations. This is a remarkable result that was not observed for certain finite-element methods [60].

6.3 Fracture of cylindrical shell

Experimental studies of detonation-driven dynamic fracture of cylindrical thin shells were reported in [61]. In the experiments a thin-walled cylindrical shell made of aluminium was attached to a rigid detonation tube. The rigid detonation tube had a length of 1.52 m and the cylindrical aluminium tube (inner radius of 1.975 cm and constant shell thickness of 0.089 cm) had a length of 89.6 cm. Different aluminium tubes with different notch lengths were studied: 2.54, 5.08 and 7.6 cm. In the experiment, Chao [61] sealed up the upper end while the lower end of the device was closed. Then, combustible gas was introduced in the tubes and thermally ignited. The combustion quickly turned into detonation. Since this is very difficult to model in numerical simulation, we modelled the detonation by pressure–time history on the inner walls of the cylinder as given by [61]. Rabczuk et al. [62] carried out FSI-simulations of those experiments and noted that it is crucial to take into account the effects due to fluid–structure interaction. When the same load is applied to all three specimens with different notch lengths it is not possible to predict or replicate the experimental data of [61]. Therefore, the loading has to vary in those experiments as also noticed of [61]. Since the loading, i.e., the pressure–time history is difficult to measure experimentally, a full coupled FSI simulation is highly desirable. Although we were not able to fully cover all major fracture mechanisms observed Chao [61], the qualitative agreement between our uncoupled simulations and the experiments using the loads as recommended Chao [61] is still sufficient, also concerning the extensive computational costs for fully coupled simulations. This aspect will be studied in the future.

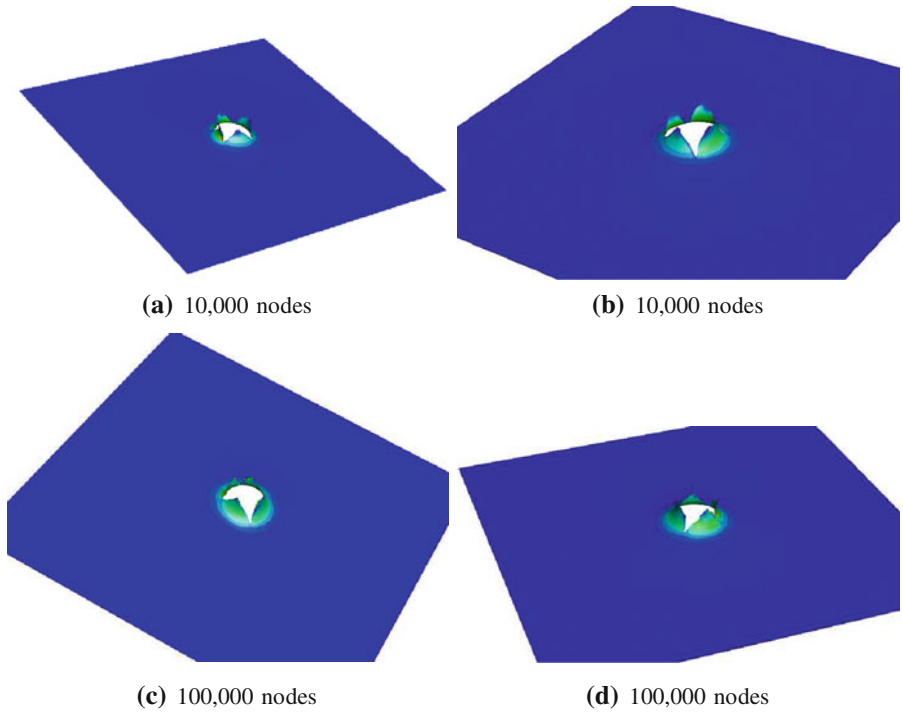

(a) 10,000 nodes **(b)** 10,000 nodes

(c) 100,000 nodes **(d)** 100,000 nodes

Fig. 10 Displaced plate for two different meshes after having been impacted by a spherical projectile

The material parameters for the aluminium tube are: density $\varrho = 2780.0\,\mathrm{kg/m^3}$, Young modulus $E = 69.0$ GPa, Poisson ratio = 0.30, yield stress of 275.0 MPa.

6.3.1 2.54 cm notch

Cracks propagated from the tips of the pre-notch in the axial direction before the crack moving towards the location of ignition slightly curves and propagates in the combined axial/circumferential direction. This crack propagates only a short distance in the circumferential direction. The other crack is arrested soon. The deformed configuration at the end of the simulation is shown in Fig. 11a, c and compares well to the experimental failure pattern (Fig. 12a).

6.3.2 5.08 cm notch

Cracks again propagate initially straight in the axial direction before they start branching and both propagate mainly in the circumferential direction. The circumferential cracks propagate a long distance but do not fragment the tube; see Fig. 11e, f. The experimental crack pattern was similar although one side of the tube did not branch; see Fig. 12b. Overall, this failure pattern is predicted with sufficient accuracy.

6.3.3 7.68 cm notch

Again, cracks propagate from the tips of the pre-notch in a straight line in the axial direction. Then, both cracks branch and change direction mainly in a circumferential direction. This time they encompass the entire circumference and fragment the tube into three large pieces. The middle piece contains many smaller internal cracks. Also, the tube in the experiment showed this behavior, meaning it was divided into three larger pieces and the middle piece

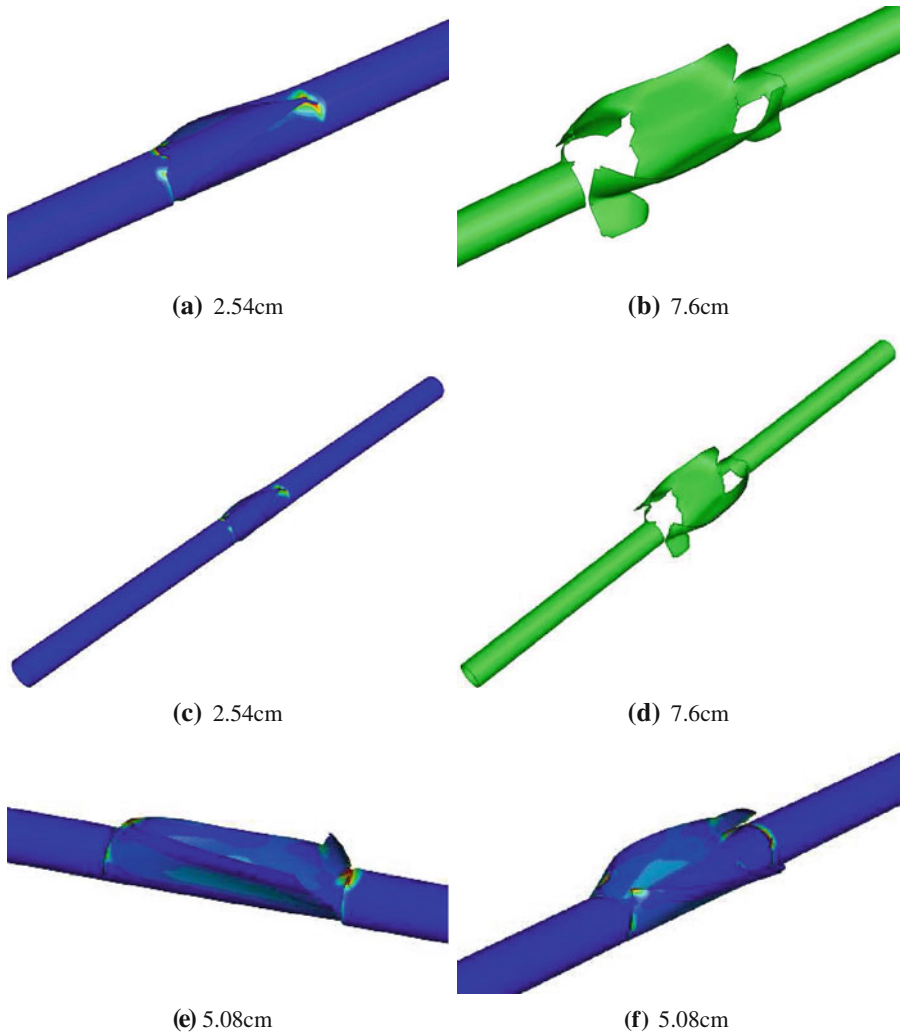

(a) 2.54cm **(b)** 7.6cm

(c) 2.54cm **(d)** 7.6cm

(e) 5.08cm **(f)** 5.08cm

Fig. 11 Displaced configuration of cylindrical shell

contained internal cracks. The displaced tube at the end of the simulation is shown in Fig. 11b, d. It is shown next to the tube with the short notch to emphasize the difference. A complete failure was also observed in the experiments (Fig. 12c).

6.4 Cylinder under internal pressure

The last example is a cylinder under internal pressure; see Fig. 13 for the configuration. The axial length of the cylinder is 1.2 m, mean radius is 22.575 cm and thickness 0.15 cm. The cylinder is clamped at both ends and was studied previously by other authors [63,64], so we have results to compare with. The discretization for 30,000 nodes and 150,000 nodes is shown in Fig. 14; the mesh is only created for illustration purposes; the method is purely meshfree. We have chosen this problem since different failure mechanisms occur at different load rates, i.e., a single crack grows at static load while crack branching occurs under dynamic load. We check whether our method is capable of capturing this phenomenon. Therefore, we increased the internal pressure linearly: for the slow load

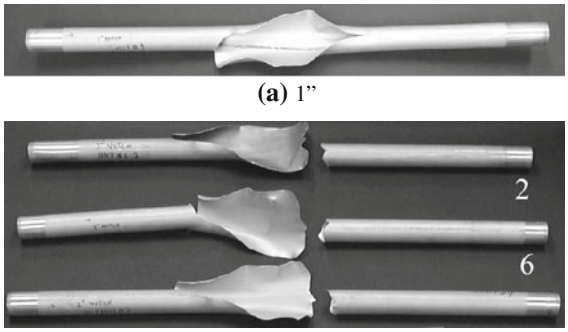

(a) 1”

(b) 2”

(c) 2”

Fig. 12 Experimental results

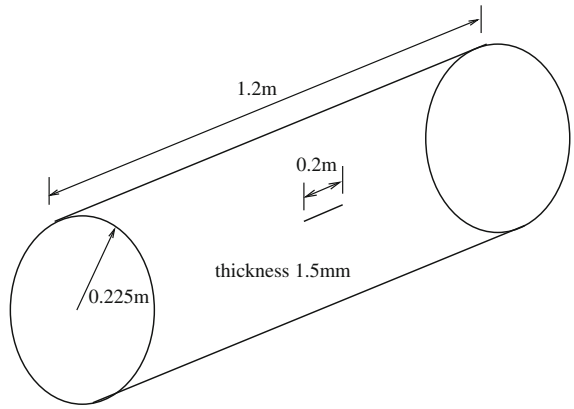

Fig. 13 Dimension of the pressurized-cylinder problem

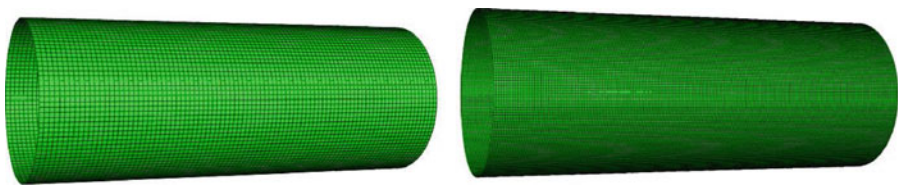

(a) 30,000 nodes **(b)** 150,000 nodes

Fig. 14 Structured nodal arrangement and background mesh of the pressurized-cylinder problem; initial configuration

rate, the pressure is increased at a rate of 15.2 Pa/s and for the fast load rate, the pressure is increased at a load rate of 15.2 kPa/s [64].

The displaced cylinder for slow load rate is illustrated in Fig. 15; see also Fig. 16 for a close-up. The crack propagates straight. For fast load rate, the crack propagates first straight but then branches. This was also observed by other authors [46,65–68]. The maximum radial displacements measured from the simulation data for different meshes are shown in Fig. 17. They converge towards a constant value. The displaced cylinder and the crack patterns are also very similar and therefore we conclude that our method can capture the basic phenomenon of branching cracks independent of the discretization. Figure 15 shows the displaced cylinder for the simulation with 100,000 particles. The results agree well with the results obtained by other authors.

7 Conclusion

The fracture of thin-walled structures was studied with the SPH shell formulation based on the Mindlin–Reissner theory. Therefore, the continuum SPH formulation is modified such that the behavior of the shell is determined using a model discretized only on the mean surface alone. The mean surface consists of a single layer of particles in which each point on the mean plane is assigned a thickness that varies in space and time. Correction and stabilization of the classical SPH formulation is adopted from [13]. Moreover an elasto–plastic constitutive model is employed for the SPH shell in the bulk while a discrete-crack method is used to model fracture. Therefore, we have presented an effective method to describe the discontinuous displacement field based on a simple node-splitting algorithm. The Rankine criterion is used for crack propagation, although more-realistic fracture methods based on enrichment and

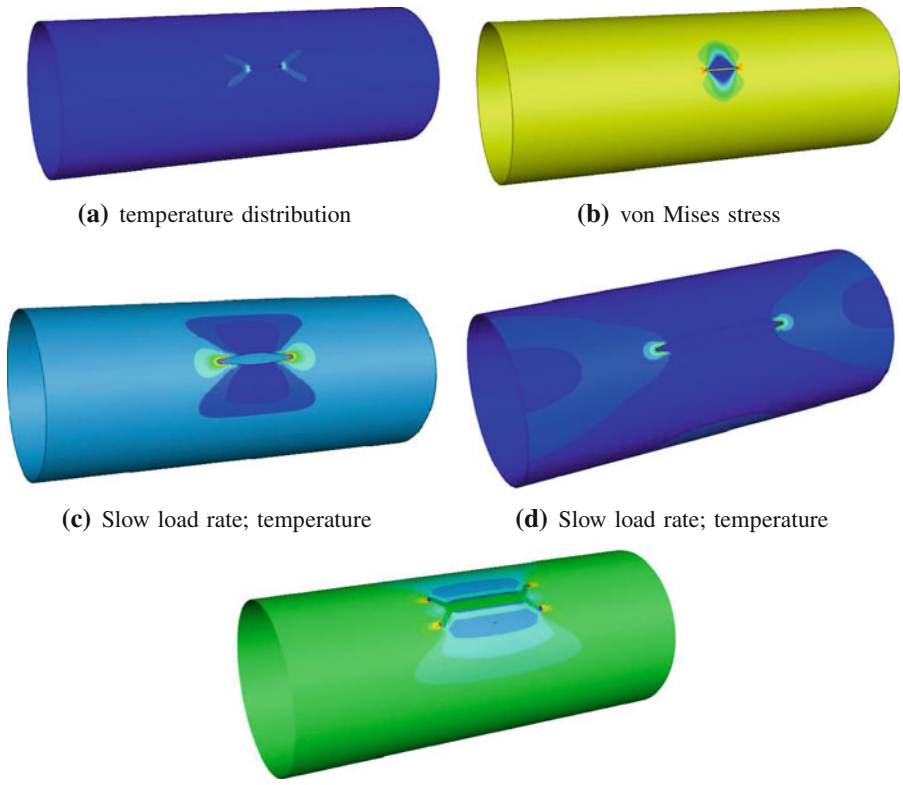

(a) temperature distribution **(b)** von Mises stress

(c) Slow load rate; temperature **(d)** Slow load rate; temperature

(e) Fast load rate; von Mises stress

Fig. 15 Displaced configuration of the cylinder under internal pressure

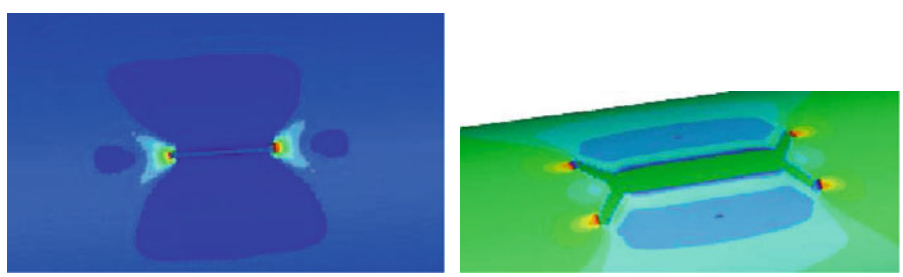

(a) **(b)**

Fig. 16 Close-up of the crack

cohesive models [69,70] will be implemented in the future in order to reach our final goal: a robust and accurate simulation of dynamic fracture in thin structures. The main characteristics of our method is its robustness, simplicity and computational efficiency.

We have studied four problems. Firstly, tearing of pre-notched plates was considered and we showed accurate results that were independent of refinement of discretization for our method. Secondly, impact simulation is studied and we showed again that our method is not dependent on refinement of discretization. We also considered the detonation-driven fracture and experiment studied in [61]. We modeled all experiments from [61] and obtained similar fracture patterns as in their experiments. Finally, we showed that we were able to capture the complicated phenomenon of branching cracks for fast load rates. Hence, we developed a very promising and efficient method

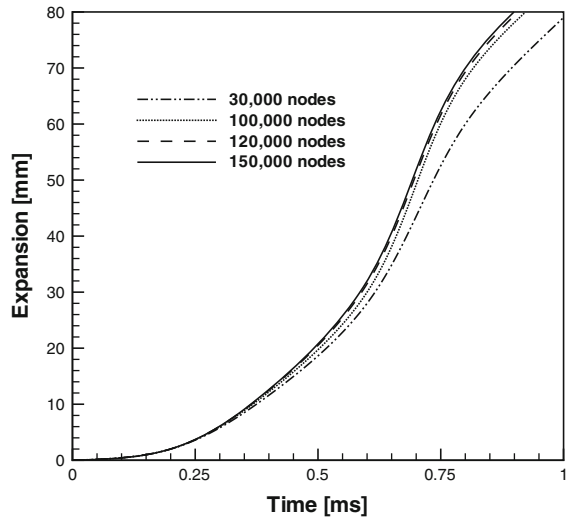

Fig. 17 Maximum radial displacements for different meshes

for dynamic fracture in thin-walled structures that will particularly be improved for fracture events: our final goal. In the future, we might develop a hybrid formulation as proposed, for instance, in the review paper [71].

References

1. Antipov YA, Willis JR (2007) Propagation of a mode-ii crack in a viscoelastic medium with different bulk and shear relaxation. J Eng Math 59:359–371
2. Lee DS (2000) Nonlinear dynamic buckling of orthotropic cylindrical shells subjected to rapidly applied loads. J Eng Math 38: 141–154
3. Johnson GR, Stryk RA (2003) Conversion of 3d distorted elements into meshless particles during dynamic deformation. Int J Impact Eng 28:947–966
4. Rabczuk T, Eibl J (2006) Modelling dynamic failure of concrete with meshfree methods. Int J Impact Eng 32:1878–1897
5. Lucy L (1977) A numerical approach to the testing of the fission hypothesis. Astron J 82:1013–1024
6. Gingold RA, Monaghan JJ (1977) Smoothed particle hydrodynamics: theory and application to non-spherical stars. Mon Not R Astron Soc 181:375–389
7. Randles PW, Libersky LD (1997) Recent improvements in SPH modeling of hypervelocity impact. Int J Impact Eng 20:525–532
8. Khayyer A, Shao SD, Gotoh H (2008) Corrected incompressible SPH method for accurate water-surface tracking in breaking waves. Coast Eng 55(3):236–250
9. Bonet J, Kulasegaram S (2000) Correction and stabilization of smooth particle hydrodynamics methods with application in metal forming simulations. Int J Numer Methods Eng 47(6):1189–1214
10. Johnson GR, Beissel SR (1996) Normalized smoothing functions for SPH impact computations. Comput Methods Appl Mech Eng 39:2127–2741
11. Vignjevic R, Campbell J, Libersky LD (2000) A treatment of zero-energy modes in the smoothed particle hydrodynamics method. Comput Methods Appl Mech Eng 184:67–85
12. Swegle JW, Hicks DL, Attaway SW (1995) Smoothed particle hydrodynamics stability analysis. J Comput Phys 116:123–134
13. Randles PW, Libersky L (2000) Normalized SPH with stress points. Int J Numer Methods Eng 48:1445–1461
14. Rodriguez-Paz M, Bonet J (2005) A corrected smooth particle hydrodynamics formulation of the shallow-water equations. Comput Struct 83(17–18):1396–1410
15. Chen J-S, Wu C-T, Yoon S, You YS (2001) A stabilized conforming nodal integration for galerkin mesh-free method. Int J Numer Methods Eng 50:435n–466
16. Wang DD, Chen JS (2006) A locking-free meshfree curved beam formulation with the stabilized conforming nodal integration. Comput Mech 39(1):83–90
17. Rabczuk T, Belytschko T, Xiao SP (2004) Stable particle methods based on lagrangian kernels. Comput Methods Appl Mech Eng 193:1035–1063
18. Beissel S, Belytschko T (1996) Nodal integration of the element-free galerkin method. Comput Methods Appl Mech Eng 139:49–74
19. Noguchi H, Kawashima T, Miyamura T (2000) Element free analysis of shell and spatial structures. Int J Numer Methods Eng 47:1215–1240

20. Rabczuk T, Areias PMA, Belytschko T (2007) A meshfree thin shell method for non-linear dynamic fracture. Int J Numer Methods Eng 72(5):524–548
21. Rabczuk T, Areias P (2006) A meshfree thin shell for arbitrary evolving cracks based on an extrinsic basis. Comput Model Eng Sci 16(2):115–130
22. Leitao VMA (2001) A meshless method for kirchhoff plate bending problems. Int J Numer Methods Eng 52:1107–1130
23. Liew KM, Chen XL (2004) Mesh-free radial point interpolation method for the buckling analysis of mindlin plates. Int J Numer Methods Eng 60:1877–1961
24. Krysl P, Belytschko T (1996) Analysis of thin shells by the element-free galerkin method. Int J Numer Methods Eng 33:3057–3078
25. Krongauz Y, Belytschko T (1997) Consistent pseudo derivatives in meshless methods. Comput Methods Appl Mech Eng 146: 371–386
26. Maurel P, Combescure A (2008) An SPH shell formulation for plasticity and fracture analysis in explicit dynamics. Int J Numer Methods Eng 75:949–971
27. Organ D, Fleming M, Terry T, Belytschko T (1996) Continuous meshless approximations for nonconvex bodies by diffraction and transparency. Comput Mech 18:225–235
28. Belytschko T, Guo Y, Liu WK, Xiao SP (2000) A unified stability analysis of meshfree particle methods. Int J Numer Methods Eng 48:1359–1400
29. Belytschko T, Krongauz Y, Organ D, Fleming M, Krysl P (1996) Meshless methods: an overview and recent developments. Comput Methods Appl Mech Eng 139:3–47
30. Dilts GA (2000) Moving least square particle hydrodynamics I. Consistency and stability. Int J Numer Methods Eng 44:1115–1155
31. Rabczuk T, Eibl J (2003) Simulation of high velocity concrete fragmentation using SPH/MLSPH. Int J Numer Methods Eng 56:1421–1444
32. Libersky L, Petscheck AG (1993) High strain lagrangian hydrodynamics. J Comput Phys 109:67–75
33. Petscheck AG, Libersky L (1994) Cylindrical sph. J Comput Phys 109:76
34. Monaghan JJ, Gingold R (1983) Shock simulation by the particle method sph. J Comput Phys 52:374–389
35. Monaghan JJ (1994) Simulating free surface flows with sph. J Comput Phys 110:399–406
36. Ilyushin AA (1956) Plasticite. Eyrolles, Paris
37. Zeng Q, Combescure A, Arnaudeau F (2001) An efficient plasticity algorithm for shell elements application to metal forming simulations. Comput Struct 7:1525–1540
38. Belytschko T, Liu WK, Moran B (2001) Nonlinear finite elements for continua and structures. Wiley, New York
39. Lubliner J (2001) Plasticity theory. Wiley, New York
40. Onate E, Owens R (2007) Computational plasticity. Springer
41. Belytschko T, Lu YY, Gu L (1995) Crack propagation by element-free galerkin methods. Eng Fract Mech 51(2):295–315
42. Belytschko T, Tabbara M (1996) Dynamic fracture using element-free galerkin methods. Int J Numer Methods Eng 39(6):923–938
43. Belytschko T, Fleming M (1999) Smoothing, enrichment and contact in the element free galerkin method. Comput Struct 71: 173–195
44. Belytschko T, Lu YY, Gu L (1994) Element-free galerkin methods. Int J Numer Methods Eng 37:229–256
45. Rabczuk T, Belytschko T (2005) Adaptivity for structured meshfree particle methods in 2d and 3d. Int J Numer Methods Eng 63(11):1559–1582
46. Rabczuk T, Belytschko T (2004) Cracking particles: a simplified meshfree method for arbitrary evolving cracks. Int J Numer Methods Eng 61(13):2316–2343
47. Xu XP, Needleman A (1994) Numerical simulations of fast crack growth in brittle solids. J Mech Phys Solids 42:1397–1434
48. Zimmermann T (1986) Failure and fracturing analysis of concrete structures. Nucl Eng Des 92(3):389–410
49. Rabczuk T, Akkermann J, Eibl J (2005) A numerical model for reinforced concrete structures. Int J Solids Struct 42(5–6):1327–1354
50. Rabczuk T, Belytschko T (2006) Application of particle methods to static fracture of reinforced concrete structures. Int J Fract 137(1–4):19–49
51. Rabczuk T, Song J-H, Belytschko T (2009) Simulations of instability in dynamic fracture by the cracking particles method. Eng Fract Mech 76:730–741
52. Rabczuk T, Zi G, Gerstenberger A, Wall WA (2008) A new crack tip element for the phantom node method with arbitrary cohesive cracks. Int J Numer Methods Eng 75:577–599
53. Rabczuk T, Areias PMA (2006) A new approach for modelling slip lines in geological materials with cohesive models. Int J Numer Anal Methods Geomech 30(11):1159–1172
54. Rabczuk T, Areias PMA, Belytschko T (2007) A meshfree thin shell method for non-linear dynamic fracture. Int J Numer Methods Eng 72(5):524–548
55. Rabczuk T, Bordas S, Zi G (2007) A three-dimensional meshfree method for continuous multiple crack initiation, nucleation and propagation in statics and dynamics. Comput Mech 40(3):473–495
56. Bordas S, Rabczuk T, Zi G (2008) Three-dimensional crack initiation, propagation, branching and junction in non-linear materials by extrinsic discontinuous enrichment of meshfree methods without asymptotic enrichment. Eng Fract Mech 75:943–960
57. Fleming M, Chu YA, Moran B, Belytschko T (1997) Enriched element-free galerkin methods for crack tip fields. Int J Numer Methods Eng 40:1483–1504

58. Nguyen VP, Rabczuk T, Bordas S, Duflot M (2008) Meshless methods: a review and computer implementation aspects. Math Comput Simul 79:763–813
59. Muscat-Fenech CM, Atkins AG (1997) Out-of-plane stretching and tearing fracture in ductile sheet materials. Int J Fract 84:297–306
60. Teng X, Rohr I, Wierzbicki T, Hiermaier S (2005) Numerical prediction of fracture in the taylor test. Int J Solids Struct 42(910):2929–2948
61. Chao TW (2004) Gaseous detonation-driven fracture of tubes. PhD thesis, California Institute of Technology
62. Rabczuk T, Gracie R, Song JH, Belytschko T (2010) Immersed particle method for fluid-structure interaction. Int J Numer Methods Eng 81:48–71
63. Li S, Hao W, Liu WK (2000) Numerical simulations of large deformation of thin shell structures using meshfree methods. Comput Mech 25:102–116
64. Qian D, Eason T, Li S, Liu WK (2008) Meshfree simulation of failure modes in thin cylinders subjected to combined loads of internal pressure and localized heat. Int J Numer Methods Eng 76:1159–1184
65. Zhou M, Ravichandran G, Rosakis AJ (1996) Dynamically propagating shear bands in impact-loaded prenotched plates, 2. numerical simulations. J Mech Phys Solids 44(6):1007–1032
66. Ravi-Chandar K (1998) Dynamic fracture of nominally brittle materials. Int J Fract 90:83–102
67. Sharon E, Gross PSP, Fineberg J (1995) Local crack branching as a mechanism for instability in dynamic fracture. Phys Rev Lett 74:5096–5099
68. Rabczuk T, Belytschko T (2007) A three-dimensional large deformation meshfree method for arbitrary evolving cracks. Comput Methods Appl Mech Eng 196(29–30):2777–2799
69. Rabczuk T, Bordas S, Zi G (2007) A three dimensional meshfree method for static and dynamic multiple crack nucleation/propagation with crack path continuity. Comput Mech 40(3):473–495
70. Zi G, Rabczuk T, Wall W (2007) Extended meshfree methods without branch enrichment for cohesive cracks. Comput Mech 40(2):367–382
71. Rabczuk T, Xiao SP, Sauer A (2006) Coupling of mesh-free methods with finite elements: basic concepts and test results. Commun Numer Methods Eng 22(10):1031–1065